Supervised topological phase classification with Deep Neural Networks: Tutorial

Marcin Płodzień

ICFO - Institut de Ciències Fotòniques, The Barcelona Institute of Science and Technology, 08860
Castelldefels, Barcelona, Spain * CorrespondingAuthor@email.address

March 9, 2022

Abstract

Machine Learning provides an extensive range of algorithms utilized in data processing tasks which recently have found applications in the physics of condensed matter. One of the most significant challenges in topological materials is the determination of global topological invariants from local measurements. This tutorial provides an entry level introduction to the topological phases of matter and utilization of supervised machine learning methods to identify Chern numbers based on the local measurements. Solving the problem of measuring topological invariants without detailed microscopic model will enable significant advances in the physics of topological materials.

Contents

---

1 Introduction

This paragraph introduces Deep Learning and Artificial Neural Networks, a subclass of Machine Learning, an Artificial Intelligence (AI) aspect. For a detailed historical description of the progress in Deep Learning, we refer to the book by Terrence J. Sejnowski, *The Deep Learning Revolution: Machine Intelligence Meets Human Intelligence* [1]. Next, we shortly present recent overlap between Deep Neural Networks and quantum mechanics and their utilization in condensed matter systems. Finally, we briefly discuss topological phases of matter, which are the topic of the presented project.

1.1 Machine Learning and Deep Neural Networks

Deep learning is a branch of Machine Learning that has its roots in mathematics, computer science, and neuroscience. The origin of deep learning goes back to the birth of Artificial Intelligence in the 1950s, when there were two competing visions for how to create an AI: one vision was based on logic and computer programs, which dominated AI for decades; the other was based on learning directly from data, which took much longer to mature. In general, Deep learning algorithms are supposed to imitate the thinking process or to develop abstractions of the processed data, and can be used for *data classification*, *data clustering* and *predictive analytics* based on regression.

Neural networks are a set of algorithms designed to recognize patterns. Their fundamental task is to find an approximating function which maps *input* data to *output* data. To find such a function, the deep learning algorithms are not explicitly programmed but are usually supported with labeled datasets containing both *inputs* and *outputs*. The algorithm finds hidden relation between those two and creates a *universal approximator*, which eventually allows predicting unknown *output* for a known given *input*. Following [1] we briefly present milestones in the beginning of development of Deep Learning science:

- 1943 Walter Pitts and Warren McCulloch created a computer model based on the neural networks of the human brain called *threshold logic*.
- 1962 Frank Rosenblatt published *Principles of Neurodynamics: Perceptrons and the Theory of Brain Mechanisms*, which introduced a *Perceptron* modeling an artificial neuron.
- 1962 David Hubel and Torsten Wiesel published *Receptive Fields, Binocular Interaction and Functional Architecture in the Cat's Visual Cortex*, where presented for the first time response properties of single biological neurons recorded with a microelectrode.
- 1969 Marvin Minsky and Seymour Papert pointed out the computational limitations and disadvantages of a single artificial neuron.
- 1979 Geoffrey Hinton and James Anderson organized the *Parallel Models of Associative Memory* workshop in La Jolla, California, which brought together a new generation of neural network pioneers and led to publication of Hinton and Anderson's collected volume by the same title in 1981.
- 1987 The First *Neural Information Processing Systems (NIPS)* Conference and Workshop was held at the Denver Tech Center giving the boost to new development in the area of Deep Learning, Neurosience and Computer Vision.

Rapid improvement of computer power over the last three decades allowed to explode different research directions in Deep Learning and Computer Vision. Large amount of data and computational power allow for image *recognition*, *segmentation*, and *detection* of the objects

both on images and videos. This development paves the way for realizing concepts known, so far, only in Science-Fiction literature, such as self-driving cars or robots mimicking human emotions on their artificial faces. Deep Learning, with much success, is used for biological purposes, where medical doctors supported by classification algorithms can diagnose, for example, cancers in their early-stage; Deep Neural Networks can help in drug discovery and in genomics [2].

Another area revolutionized by Deep Neural Networks is related to data with temporal changes. The concept of *Recurrent Neural Network* was used in time-series analysis, which has been used in stock-market and weather forecasting with great success [3]. *Recurrent Neural Networks* are also used in *Natural Language Processing* area, where language-to-language translation and speech-to-sentence mapping is used [4].

Last but not least, we should mention the great success of Deep Neural Networks in human-machine competition, *i.e.* where machine beats human in popular games. In 1996 *Deep Blue* algorithm beats Kasparov in chess-match. However, this machine was explicitly programmed to analyze the best possible move on the chessboard. Real Deep Learning approach, based on *Reinforcement Learning* [5] was used in a GO-match in 2015. The *AlphaGo* program, developed by *DeepMind* company, for the first time, won with professional GO-players. *AlphaGo* was not explicitly programmed, but via *deep reinforcement learning* found the winning strategy explicitly using unsupervised learning. Today *deep reinforcement learning* is widely used in video games.

1.2 Deep Neural Networks and physical sciences

Machine Learning and Deep Neural networks have been applied in recent years in physical sciences, both in classical and quantum regime. Applications of Machine Learning can be found in particle physics, fluid dynamics, cosmology, many-body quantum systems, physics of new material as well in quantum computing and quantum information theory [6]. For most recent overview over the field of Machine Learning and physics we refer to works [7–9], while in the following we shortly describe most recent advances in the field.

In classical physics, one of the very recent surprising results is Neural Network extraction of the conservation laws from trajectories [10]. Authors present a machine learning algorithm for auto-discovering conserved quantities using trajectory data from unknown dynamical systems. The algorithm was able to find all conserved quantities as well as periodic orbits. Another exciting research direction is studies of classical systems with Neural Networks is a long-term prediction of chaotic dynamics [11]. Another very active field of classical physics studies is the derivation of equations describing finite-size spherical particles' kinematics in arbitrary fluid flows. Recurrent neural networks were used to study the particle's trajectory in a fluid flow [12].

In parallel to the research direction of utilization of Neural networks in classical problems, there is a boost in theoretical studies of quantum systems. One of the most crucial problems in condensed matter physics is the classification of phases of matter, and Neural Networks were used with great success to perform such a classification [13–16].

Another important concept in quantum many-body systems is the many-body wave function. For interacting many-body systems, size of the Hilbert space grows exponentially with increasing particle number. In order to simulate many-body systems on classical computers, one has to find a systematic way to prepare cutoff for the wave function to reduce its size while preserving all-important quantum properties. The auspicious directions is given by Variational Autoencoders, which are used to prepare low dimensional latent representation of many-body wave-function [17, 18].

Last, but not least, we mention the research direction focusing on designing and constructing hybrid systems containing specific physical setups combined with computer architectures

aimed at accelerating Neural-Network calculations. Such neuromorphic systems are hardware designed in order to directly mimics the neuronal network structure. The main goal of this research direction is to construct a physical realization of artificial neural networks performing fully parallel and fast operations. In [19, 20] the Authors propose and realize an optical network of nodes performing binary operations. Semiconductor microcavities provide the nonlinearity required for efficient computation in the substantial quantum light-matter coupling regime, which exhibits exciton–polariton interactions. The authors used a considered system for a pattern recognition task on the MNIST dataset and showed that the proposed neural network significantly increases recognition efficiency.

2 Topology in condensed matter

Topology is the branch of mathematics concerned with sets or spaces where some properties stay invariant under continuous deformations of those spaces. The process of stretching and bending a material is a continuous transformation while tearing or puncturing is not. In more detail, topology is the mathematical theory of spaces and continuous functions. The topology of a space is defined as a collection of all of the open sets in the space. A continuous function is defined as a mapping for which the inverse image of any open set is an open set. Two different spaces are then topologically equivalent if one can define a continuous bijection between the spaces. The aspect of topology that is of particular interest for the research presented here is the concept of topological invariants – aspects of spaces that remain unchanged by any continuous deformation of the space. The canonical example of a topological invariant is the Euler characteristic, which was originally defined for polyhedra, but in general, describes the shapes of surfaces. In simple terms, it is obtained from the number of holes in the body in question, such that the Euler characteristic of a torus (which has one hole) is different from that of a sphere (which does not have holes). More generally, the spaces do not necessarily have to be interpreted as physical coordinates, and the invariants can be more abstract.

2.1 Topological phases of matter

In the last four decades, notions on topology have become relevant in the physics of condensed matter in terms of topological phases and topological phase transitions. A common understanding of phase transitions contains the Ginzburg–Landau theory paradigm, where continuous phase transitions are related to symmetry breaking of a local order parameter across the transition. In Landau theory, phase transitions occur by a system spontaneously settling in a parameters configuration that breaks some of the symmetries obeyed by the free energy of the system; for instance, in a ferromagnetic material, the magnetic moments of its constituent atoms tend to align in some direction, breaking the overall rotational symmetry of the Hamiltonian. The breaking of symmetry in this paradigm is related to a local order parameter, which is zero above some critical temperature, and then takes a nonzero value as the symmetry is broken. This approach has in general, been highly successful in explaining the character of phase transitions, from magnetism to superconductivity. However, this paradigm was extended after discovering the quantum Hall effect [] by the concept of a Topological Phase Transition. Instead of a change of local symmetry, a system changes its topology having a global character. The most remarkable topological phases are quantum Hall systems, topological insulators, and topological superconductors [**?**, **?**, **?**].

The topology of the phases is encoded in the quantum-mechanical operators acting on a corresponding Hilbert space. Topologically inequivalent phases are described by Hamiltonians that cannot be continuously transformed to each other without closing the gap, *i.e.* the energy difference between ground and excited state of the system. Properties of the system

can be visualized via topological phase diagrams where between all different phases, there is a boundary with zero energy in the corresponding spectrum diagram. Topologically distinct phases have certain properties that stay invariant under continuous transformations, called topological invariants. Topological invariants can only take on integer values and change only change when moving between topologically distinct spaces and cannot change under continuous transformations remaining in a topologically equivalent space. Topological phases have then intrinsic robustness, meaning that any continuous transformation (or a small perturbation) will not eliminate the underlying topology. The robustness against changes in the topological phase makes these topological materials interesting for applications in quantum computing, where the biggest issue is sustaining the interplay between phases of matter which is so easily lost due to quantum decoherence, where quantum properties crucial from the point of quantum computing (such as entanglement) are lost. Thus, studying topological matter is not only interesting from the point of view of fundamental research; it could offer breakthroughs in quantum information processing.

Recent years bring Deep Neural networks in the topological matter, where Neural Networks were used to predict topological invariants. Networks are fed with training Hamiltonians as input and neural networks can predict topological invariants with accuracy close to or higher than 90% [21–23]. However, extracting topological invariants from an local measurements its still a demanding tasks.

2.2 Berry Phase, Berry Curvature and Chern number

In this section, we present basics concepts of topological band theory and define the Chern number, being the topic of studies in the thesis. For a detailed discussion, we refer to [**?**].

The fundamental concept of topological band theory is the Berry phase, related to adiabatic change of the quantum system. In principle, the adiabatic transport of particles in slowly varying fields (such as magnetic or electric field) could change the phase of the wave-function different from the dynamical phase. It was realized that the Berry phases should be present in systems where the parameters of the Hamiltonian are varied over closed loops, such as the Brillouin zone, by applying electric fields.

Let us consider a general time-dependent physical system $H(\mathbf{R})$ parametrized by set of parameters $\mathbf{R}$ depending on time, *i.e.* $\mathbf{R}(t) = \mathbf{R}$. We are interested in the system evolution during slow change of parameters $\mathbf{R}$ along path $\mathcal{C}$ (closed or open) in the parameters space. Let us introduce an instantaneous orthonormal basis of the Hamiltonian for each set of parameters $\mathbf{R}$:

$$H(\mathbf{R})|n(\mathbf{R})\rangle = E_n(\mathbf{R})|n(\mathbf{R})\rangle. \tag{1}$$

Our aim is to analyze phase of the wave function initially prepared in state $|n(\mathbf{R}(t)\rangle$ during slow change (slow compared to any other energy scale in the system) of $\mathbf{R}(t)$ along path $\mathcal{C}$. While we start with the instatnenous eigenstate of the Hamiltonian the only remaining degree of freedom is global phase so the wave function of the system will have a form $|\psi(t)\rangle = e^{-i\theta(t)}|n(\mathbf{R}(t)\rangle$. Time evolution of the system is given by Schrödinger equation:

$$i\hbar\frac{d}{dt}|\psi(t)\rangle = H(\mathbf{R}(t))|\psi(t)\rangle. \tag{2}$$

Substituting $|\psi(t)\rangle$ into above equation, and taking the scalar product with $\langle\mathbf{R}(t)|$, we get:

$$E_n(\mathbf{R}(t)) - i\hbar\langle n(\mathbf{R}(t))|\frac{d}{dt}|n(\mathbf{R}(t))\rangle = \hbar\frac{d}{dt}\theta(t). \tag{3}$$

Thus, solution for $\theta(t)$ is

$$\theta(t) = \frac{1}{\hbar}\int_0^t E_n(\mathbf{R}(t'))dt' - i\int_0^t \langle n(\mathbf{R}(t'))|\frac{d}{dt'}|n(\mathbf{R}(t'))\rangle. \tag{4}$$

The first part is called dynamical phase and is related only to instantaneous eigenvalues of the Hamiltonian, while the negative of the second part

$$\gamma_n = i\int_0^t \langle n(\mathbf{R}(t'))|\frac{d}{dt'}|n(\mathbf{R}(t'))\rangle dt' \tag{5}$$

is called the Berry phase and depends on the trajectory $\mathcal{C}$ in the parameter space $\mathbf{R}$ parametrized by time t. Explicit time-dependence can be removed via

$$\gamma_n = i\int_0^t \langle n(\mathbf{R}(t'))|\nabla_{\mathbf{R}}|n(\mathbf{R}(t'))\rangle \frac{d\mathbf{R}}{dt'}dt' = i\int_{\mathcal{C}} \langle n(\mathbf{R})|\nabla_{\mathbf{R}}|n(\mathbf{R})\rangle d\mathbf{R}. \tag{6}$$

In analogy to the electron transport in an electromagnetic field, we can define a vector function called Berry connection (or Berry potential):

$$\mathbf{A}_n(\mathbf{R}) = i\langle n(\mathbf{R})|\frac{\partial}{\partial \mathbf{R}}|n(\mathbf{R})\rangle = i\langle n(\mathbf{R})|\nabla_{\mathbf{R}}|n(\mathbf{R})\rangle, \tag{7}$$

and now Berry phase reads

$$\gamma_n = \int_{\mathcal{C}} d\mathbf{R}\cdot\mathbf{A}_n(\mathbf{R}). \tag{8}$$

When we consider closed paths $\mathcal{C}$ in the parameter space, that after long period T we return to its initial state $\mathbf{R}(0) = \mathbf{R}(T)$. The Berry vector potential $\mathbf{A}_n(\mathbf{R})$ is gauge dependent, *i.e.* under the change

$$|n(\mathbf{R})\rangle \to e^{i\eta(\mathbf{R})}|n(\mathbf{R})\rangle, \tag{9}$$

we have

$$\mathbf{A}_n(\mathbf{R}) \to \mathbf{A}_n(\mathbf{R}) - \frac{\partial}{\partial \mathbf{R}}\eta(\mathbf{R}), \tag{10}$$

and Berry phase will be changed by

$$-\int_{\mathcal{C}} \frac{\partial}{\partial \mathbf{R}}\eta(\mathbf{R})\cdot d\mathbf{R} = \eta(\mathbf{R}(0) - \eta(\mathbf{R}(T)). \tag{11}$$

Now, we know that after closing the loop in the parameters space the final state of the systems should be the same as the initial state, *i.e.*

$$|n(\mathbf{R}(t)) = |n(\mathbf{R}(0)\rangle, \tag{12}$$

so gauge transformation must maintain this property, *i.e.*

$$e^{i\eta(\mathbf{R}(0))}|n(\mathbf{R}(0))\rangle = e^{i\eta(\mathbf{R}(T))}|n(\mathbf{R}(T))\rangle = e^{i\eta(\mathbf{R}(0))}|n(\mathbf{R}(0))\rangle, \tag{13}$$

hence $\eta(\mathbf{R}(0) - \eta(\mathbf{R}(T)) = 2\pi m$, with m being an integer. It means that Berry phase cannot be canceled over a closed path unless it is integer itself.

Next, let us consider a closed path in a three dimensional parameter space $\mathbf{R} = (R_1, R_2, R_3)$. After application of the Stokes theorem we can change the integration over a closed contour into the integration over a surface, *i.e.*

$$\begin{aligned}
\gamma_n &= -\mathrm{Im}\int d\mathbf{S}\cdot(\nabla\times\langle n(\mathbf{R})|\nabla|n(\mathbf{R})\rangle) \\
&= -\mathrm{Im}\int dS_i\epsilon_{ijk}(\nabla_j\times\langle n(\mathbf{R})|\nabla_k|n(\mathbf{R})\rangle) \\
&= -\mathrm{Im}\int d\mathbf{S}\cdot(\langle\nabla n(\mathbf{R})\times|\nabla n(\mathbf{R})\rangle),
\end{aligned} \tag{14}$$

where we can define the Berry curvature

$$\Omega_n(\mathbf{R}) = \nabla \times \langle n(\mathbf{R})|\nabla_{\mathbf{R}}|n(\mathbf{R})\rangle) = \nabla \times \mathbf{A}_n(\mathbf{R}). \tag{15}$$

In general parameter space (non three dimensional) we define Berry curvature as a tensor:

$$\Omega_{n,\mu,\nu} = \frac{\partial}{\partial R_\mu} A_{n,\nu}(\mathbf{R}) - \frac{\partial}{\partial R_\nu} A_{n,\mu}(\mathbf{R}). \tag{16}$$

One can interpret Berry curvature $\Omega_{\mathbf{n}}(\mathbf{R})$ as a magnetic field in the parameter space, being the curl of the Berry vector potential $\mathbf{A}(\mathbf{R})$.

Finally, we can define the Chern number in the context of topological band theory. Let us consider a two-dimensional system represented in momentum space $\mathbf{k} = (k_x, k_y)$ given by Hamiltonian $H(\mathbf{k})$. One of the most important consequences of having non-trivial topological properties is the occurrence of surface states at the interface between two materials with different Berry properties (which are topologically different). The topological classification of a system is determined by the Chern number defined as the integral of the Berry curvature over momentum space,

$$C = \frac{1}{2\pi} \int_S dS \cdot \Omega_n(\mathbf{k}), \tag{17}$$

where n denotes given energy band of the system.

The aim of the presented project is to use Deep Neural Network method for extraction of the Chern number from synthetic experimental data containing information about existence (or not) edge states if finite system.

3 Artificial two-band topological Hamiltonian

In this paragraph, we provide the definition of the artificial topological Hamiltonian which realizes arbitrary Chern number. Next, we discuss the relation between topological invariant to the *edge* states appearing in finite-size systems, which are localized at the boundaries of the finite systems.

3.1 Bulk Hamiltonian

We consider the model of the artificial two-dimensional, two-band Hamiltonian supporting an arbitrary Chern number. In momentum representation, *i.e.* $\mathbf{k} = (k_x, k_y) \in [-\pi, \pi) \times [-\pi, \pi)$ considered Hamiltonian reads:

$$H(\mathbf{k}) = \begin{pmatrix} \xi_\alpha(\mathbf{k}) & \Delta_N(\mathbf{k}) \\ \Delta_N^*(\mathbf{k}) & -\xi_\alpha(\mathbf{k}) \end{pmatrix}, \tag{18}$$

where the diagonal elements read:

$$\xi_\alpha(\mathbf{k}) = (1-\alpha)\xi^{(nn)}(\mathbf{k}) + \alpha\xi^{(nnn)}(\mathbf{k}), \tag{19}$$

with

$$\begin{aligned} \xi^{(nn)}(\mathbf{k}) &= -2(\cos(k_x) + \cos(k_y)) - \mu \\ \xi^{(nnn)}(\mathbf{k}) &= -2(\cos(k_x + k_y) + \cos(k_x - k_y)) - \mu. \end{aligned} \tag{20}$$

and off-diagonal elements read:

$$\begin{aligned} \Delta_N(\mathbf{k}) &= |\Delta_{\mathbf{k}}| e^{iN\arg(\Delta_{\mathbf{k}})} \\ \Delta_{\mathbf{k}} &= \sin(k_x) + i\cos(k_y). \end{aligned} \tag{21}$$

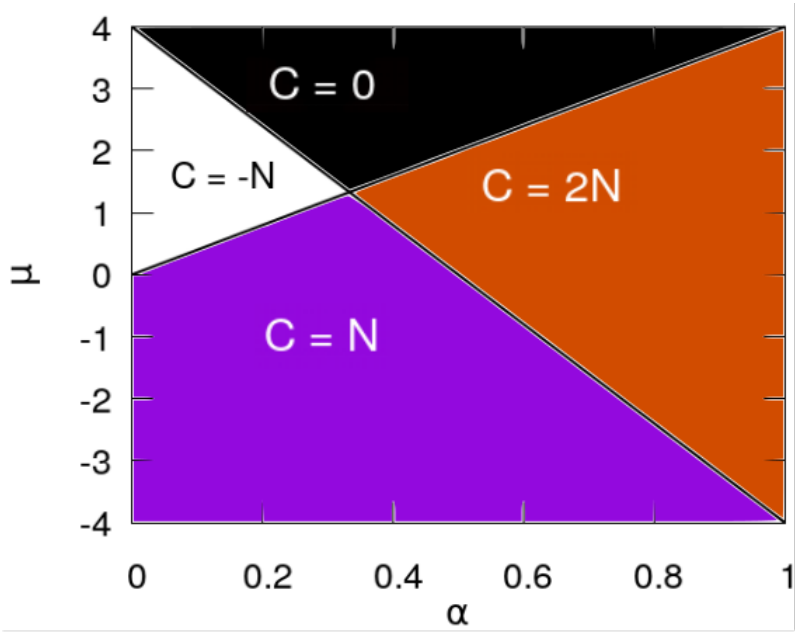

Figure 1: Topological phase diagram of the artificial topological Hamiltonian, eq.(18) realizing arbitrary Chern number C.

The presented model is artificial, however we can provide a physical interpretation of its elements. The dispersion relation parametrized by α, contains term $\xi^{(nn)}(\mathbf{k})$ being the nearest-neighbour hopping and $\xi^{(nnn)}(\mathbf{k})$ being the next-nearest neighbour hopping and μ is the chemical potential, while $\Delta_N(\mathbf{k})$ stands for superconducting order parameter. The free parameters of the model are *i.e.* $\alpha \in [0,1)$ and $N \in \mathbb{N}$, and determine the Chern number for the lower band, *i.e.* $C = C(\alpha, \mu, N)$. Figure 1 presents the topological phase diagram of the lower band in $(\alpha - \mu)$ phase-space. The border between topological phases described by distinct Chern numbers C is given by vanishing band gap, *i.e.* when for a given pair $\{\alpha, \mu\}$ the condition

$$\delta_0 = \min_{(k_x,k_y)} \sqrt{\xi_\alpha^2(k) + |\Delta(k)|^2} = 0 \tag{22}$$

is met. Such a situation,*i.e.* when topological invariant changes its value under the change of the model parameters, is called *topological phase transition*.

3.2 Bulk-boundary correspondence and edge states

The bulk-boundary correspondence sets a relation between a bulk property of a *closed geometry* model given by a topological invariant (Chern number) and several states living only on the boundaries of the finite system. For topological phases of the model, with $C \neq 0$, in the bandgap appear loe-energy states which are localized near boundaries of the sample, and not in bulk - these are called *edge* states. The number of such states in the system is given by the absolute value of the Chern number $|C|$.

To obtain edge states and visualize the bulk-boundary correspondence, we express the momentum space Hamiltonian, eq.(18), in real space. To break periodicity of the system in y direction, first let us define n-th Fourier component of the Hamiltonian, eq.(18), in k_y-direction:

$$h_n(k_x) = \frac{1}{2\pi} \int_{-\pi}^{\pi} e^{-ik_y n} H(k_x, k_y) dk_y. \tag{23}$$

Next, we can construct Hamiltonian representation in geometry where we consider N_y sites

of the lattice in y direction preserving momentum space representation in x direction:

$$H_{N_y}(k_x) = \begin{bmatrix} h_0(k_x) & h_1(k_x) & h_2(k_x) & \dots \\ h_{-1}(k_x) & h_0(k_x) & h_1(k_x) & \dots \\ \dots & \dots & \ddots & \dots \\ \dots & h_{-2}(k_x) & h_{-1}(k_x) & h_0(k_x) \end{bmatrix}, \tag{24}$$

where number of diagonal elements equals to N_y. In this case we preserve periodicity in k_x space while we break periodicity in y direction - and we call this system as *half-opened geometry*, where wave-function depends on momentum k_y and given position $y \in [0, N_y]$ on a lattice.

Similar construction can be provided in order break periodicity in x direction, *i.e.* we define m-th Fourier component of $H_{N_y}(k_x)$ as:

$$g_m = \frac{1}{2\pi} \int_{-\pi}^{\pi} e^{-ik_x m} H_{N_y}(k_x) dk_x, \tag{25}$$

and construct real space representation of original Hamiltonian eq.(18) on a square lattice with size $N_x \times N_y$ as:

$$H_{N_x,N_y} = \begin{bmatrix} g_0 & g_1 & g_2 & \dots \\ g_{-1} & g_0 & g_1 & \dots \\ \dots & \dots & \ddots & \dots \\ \dots & g_{-2} & g_{-1} & g_0 \end{bmatrix}, \tag{26}$$

where number of diagonal elements equal to N_x. This case we will call *fully-opened geometry* where each wave-function depends on (x, y) position on a square finite lattice.

Having obtained real-space representation of the considered model we solve eigenproblem for real-space representation H_{N_x,N_y}, *i.e.* we solve equation

$$H_{N_x,N_y}|\psi_i(x,y)\rangle = E_i|\psi_i(x,y)\rangle = E_i \begin{bmatrix} |\psi_i^u(x,y)\rangle \\ |\psi_i^d(x,y)\rangle \end{bmatrix}, \tag{27}$$

and obtain eigenstates $|\psi_i(x,y)\rangle$ with eigenenergies E_i. Eigenspectrum $\{E_i\}$ has particular properties:

1. spectrum is symmetric around $E = 0$,
2. spectrum has two bands separated by band gap energy δ_0.

Each eigenstate has two components: $|\psi_i^u(x,y)\rangle$ corresponding to upper band and $|\psi_i^l(x,y)\rangle$ corresponding to lower band. For topologically trivial phases, there are no states in the bandgap. However, for geometries with boundaries, (*half-opened* or *fully-opened*), phases with non-zero Chern number $C \neq 0$ have low-energy states in the middle of the bandgap which are localized on the boundaries of the system. Figure 2 presents spectrum for topologically trivial phase with $C = 0$ with bulk states (top panel) and spectrum of topologically non-trivial phase with $C = 1$ (bottom panel). Figure 3 presents *bulk states* (living in the whole lattice) and topological *edge state* living only at the boundaries.

In order to take into account not only a single state, we define the Local Density of States (LDOS) defined as

$$\rho(x,y) = \frac{1}{\mathcal{N}} \sum_{E_i \in \mathcal{E}} |\psi_i^u(x,y)|^2 + |\psi_i^l(x,y)|^2, \tag{28}$$

where we sum over states with energies E_i from a given energy window $\mathcal{E} = 0.1\delta_0$. Normaliza-

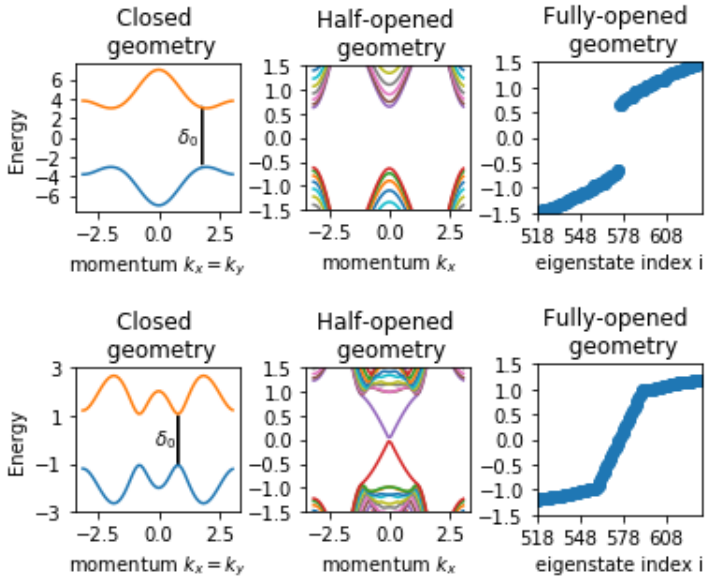

Figure 2: Left panel: spectrum of the model Hamiltonian for *closed*, *half-opened* and *fully-opened* geometries for topologically trivial phase with Chern number $C = 0$ ($\alpha = 0.6$, $\mu = 3$, $N = 1$). There are distinct energy bands separated by band gap energy δ_0 with no states around $E = 0$. Right panel: spectrum of topologically non-trivial phases in three geometries with Chern number $C = 1$ ($\alpha = 0.6$, $\mu = -2$, $N = 1$). There appear topological states, living on the boundaries of the sample, connecting upper and lower energy bands. These are called *edge states*.

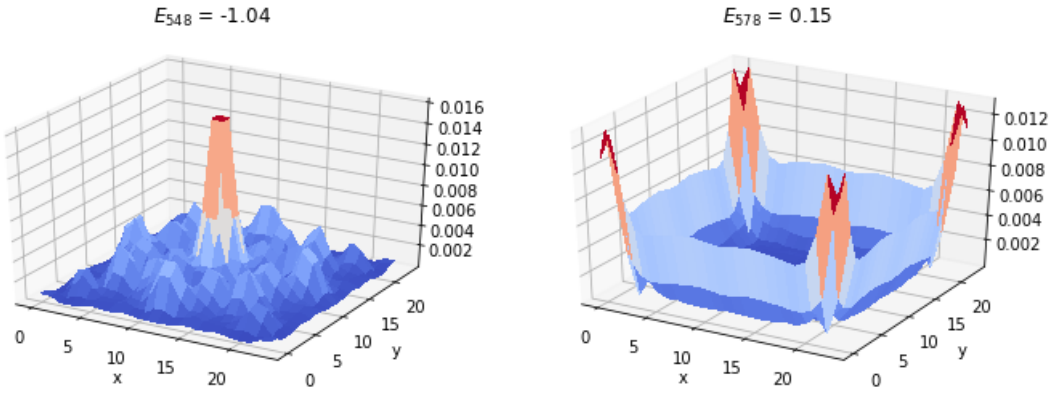

Figure 3: Examples of probability density $|\psi_i^d(x,y)|^2 + |\psi_i^l(x,y)|^2$ of the *bulk state* (left panel) and *edge state* (right panel) in *fully-opened geometry* for topological phase characterized by Chern number $C = 1$ ($\alpha = 0.6, \mu = -2, N = 1$). Lattice size is 24×24.

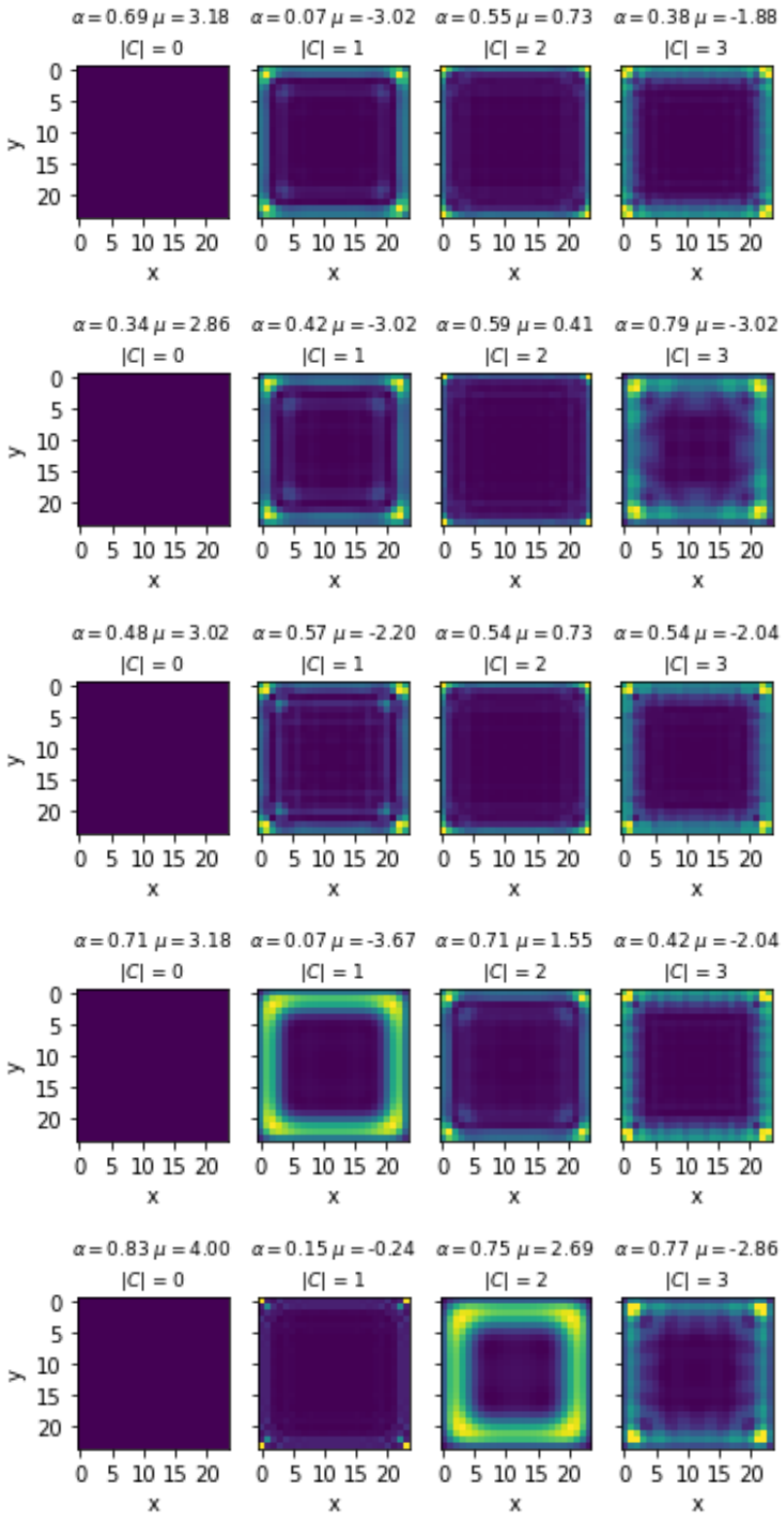

Figure 4: Local Density of States (with energy window $\mathcal{E} = 0.1\delta_0$) for clean system. Clearly for $C = 0$ there are no in-gap states, thus LDOS is zero everywhere. For non-zero C *edge* states appear at the system boundaries.

tion constant $\mathcal{N}$ gives $\int \rho(x,y)dxdy = 1$, and thus LDOS has interpretation of a probability density of finding a particle at point (x,y). Figure 4 presents LDOS for different Chern numbers C obtained for *fully-opened* geometry on square lattice with size 24×24. There are an evident distinction between non-topological states $C = 0$ and topological states with $C \neq 0$; however, the distinction between LDOS for non-zero C is not trivial.

3.3 Edge states in the presence of disorder

So far, we have discussed only perfect clean systems without any imperfections. When we want to consider imperfections in the finite system, we should characterize the topological phase of matter in real space. The definition of the Chern number C is valid for an infinite (periodic) system described in momentum space, however, there exists a systematic way of providing topological invariant in real space given by Local Chern Marker [**?**]. Local Chern Marker may vary from site-to-site for the finite system; thus, we consider the mean-value of the Local Chern Marker averaged over lattice denoted by C_m. This approach allows us to characterize topological phases in the presence of local imperfections. We consider situation where to real-space Hamiltonian, eq.(26), we add on-site random potential $V(x,y)$ taken from uniform distribution $V(x,y) \in V_0\left[-\frac{1}{2},\frac{1}{2}\right]$, where V_0 is disorder amplitude measured in the units of clean system gap δ_0.

Figure 5 presents LDOS for different point on phase diagram for disorder amplitudes $V_0/\delta_0 = \{0, 0.2, 0.4, 0.6, 0.8\}$ together with accompanying Chern marker C_m. Combination of the finite-size effects together with the presence of the disorder potential can significantly affect Chern marker C_m, which can strongly deviate from bulk Chern number C as well as LDOS has large fluctuations from shot-to-shot realization. Additionally, a disorder potential can create bulk states appearing in the bandgap (left column). In order to quantitatively study impact of the disorder on the topologiacal invariants, we show in Figure 6 the dependence of the Chern marker C_m against disorder amplitude V_0 averaged over 50 realizations of the random potential. On average, the Chern marker and Chern number are close to each other for $V_0/\delta_0 < 1$, while the above critical value of V_0/δ_0 Chern marker decays with disorder amplitude, indicating that perturbations due to disorder potential destroy topological properties in the finite system.

At this moment, we can define our problem: we would like to train, within a supervised manner, a Deep Neural Network model which can predict the absolute value of the bulk Chern number $|C|$ based on Local Density of States measurements in the finite system including imperfections of a given sample, modeled by the presence of disorder potential. Because our input data contains information only about densities, and there is no information about the phase of the wave functions, we can predict only the absolute value of the bulk Chern number $|C|$.

4 Data generation

In this paragraph, we discuss in a systematic way the data generation procedure, define three Neural Networks architectures and compare their performance in Chern number identification as a function of the disorder amplitude.

In the first step we cover the $(\alpha - \mu)$ phase diagram, Figure 1, with a grid of 25×25 sampling points. For each pair $\{\alpha, \mu\}$ for a given $N = 1, 3$ we calculate local band gap $\delta_0 = \min_{kx,ky} \sqrt{\xi_\alpha^2(k) + |\Delta(k)|^2}$ and absolute value of the bulk Chern number $|C|$. Next, we diagonalize the real-space Hamiltonian, eq.(26) on a two-dimensional finite lattice $N_x \times N_y$, $N_x = N_y = 24$ for each tuple of parameters $\{\alpha, \mu, N, V_0\}$, where $V_0/\delta_0 = \{0, 0.1, 0.2, 0.3, ..., 1.9\}$ is amplitude of the disordered potential. For given set of eigenvalues E_i and eigenvectors

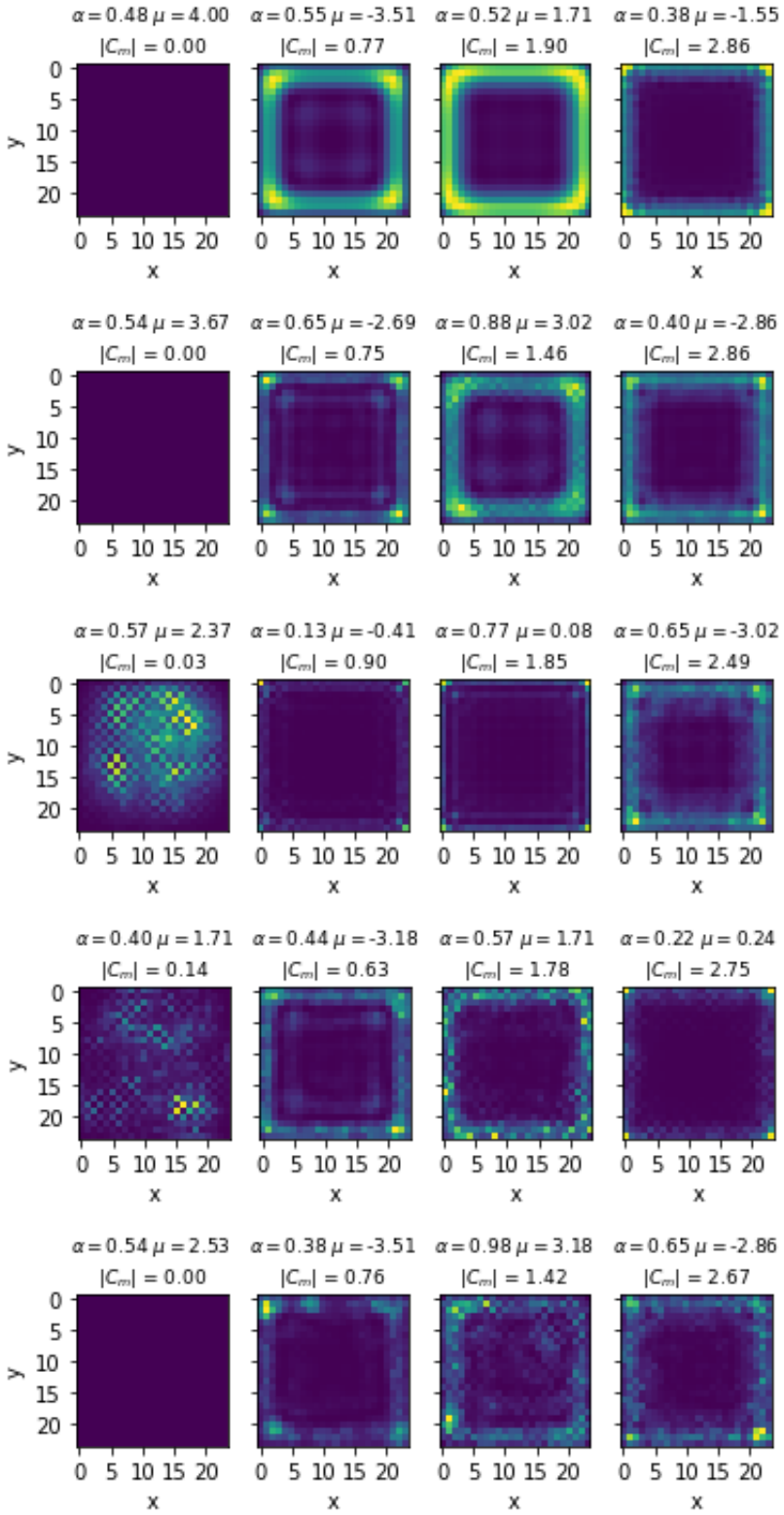

Figure 5: Local Density of States in the presence of disorder potential with amplitude $V_0/\delta_0 = \{0, 0.2, 0.4, 0.6, 0.8\}$ (panels from top to bottom). Presence of the disorder potential can significantly affects the Chern marker C_m which deviates from bulk Chern number C. Additionally, presence of the disorder can result in appearing in-gap bulk states (left column).

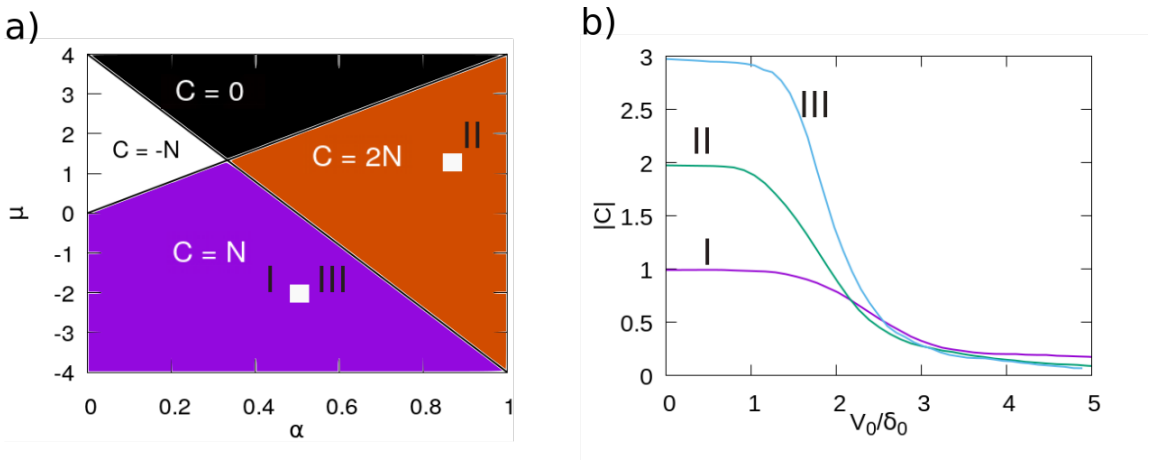

Figure 6: a) Topological phase diagram of the spectrum-symmetric topological toy-model, eq.(18) realizing arbitrary Chern number C. b) Robustness of the Chern marker C against on-site disorder amplitude V_0 measured in units of mean bulk energy gap δ_0 for finite system size $N_x = N_y = 24$.

$|\psi_i(x,y)\rangle$ we calculate absolute value of the Chern marker $|C_m|$ and Local Density of States

$$\rho(x,y) = \frac{1}{\mathcal{N}} \sum_{E_i \in \mathcal{E}} |\psi_i(x,y)|^2, \tag{29}$$

with energy window $\mathcal{E}$ being 10% of the averaged clean system gap δ_0. Normalization constant $\mathcal{N}$ is chosen in such a way that $\int \rho(x,y)dxdy = 1$. In the last step we rescale each LDOS as $\rho(x,y) \to \overline{\rho}(x,y) = \rho(x,y)/\mathrm{std}(\rho(x,y))$. We repeat the above procedure for 10 realizations of the disorder potential with a given amplitude V_0, generating *raw dataset* containing 85570 tuples of $\{\alpha, \mu, \delta_0, V_0, |C|, |C_m|, \overline{\rho}(x,y)\}$. Figure 7 (top panel) presents histogram of the absolute values of the generated Chern markers $|C_m|$ at finite square lattice 24×24 with disorder potential in *raw dataset*. Each distribution belongs to the given bulk Chern number $|C|$ in an infinite clean system. Chern markers distributions possess heavy overlaping tails, which comes from Hamiltonian diagonalization on finite lattice, and presence of the disorder potential. In the particular distribution of the Chern marker for Chern number $|C| = 3$ has heavy left-tail which overlap with other Chern markers distribution.

From *raw dataset* we extract *training dataset* (Chern marker histogram in Figure 7 - middle panel), and *validating dataset* containing tuples $\{X, y\}$, where $X = \overline{\rho}(x,y)$ is a input for neural network and $y = |C|$ is a corresponding label of a given category, being a *one-hot-encoded* bulk Chern number $|C|$. *Training* and *validating datasets* contain 28907 and 3613 samples, respectively, and fulfill two conditions:

1. $|C - C_m| < 0.5$,
2. $V_0 < 1$.

The above restrictions assure that Chern markers are close to bulk Chern numbers, and corresponding *LDOS* provide correct information about edge states. In the last step, we extract *testing dataset* (Figure 7 - bottom panel) containing 8151 samples that have no restriction about Chern markers and disorder amplitudes.

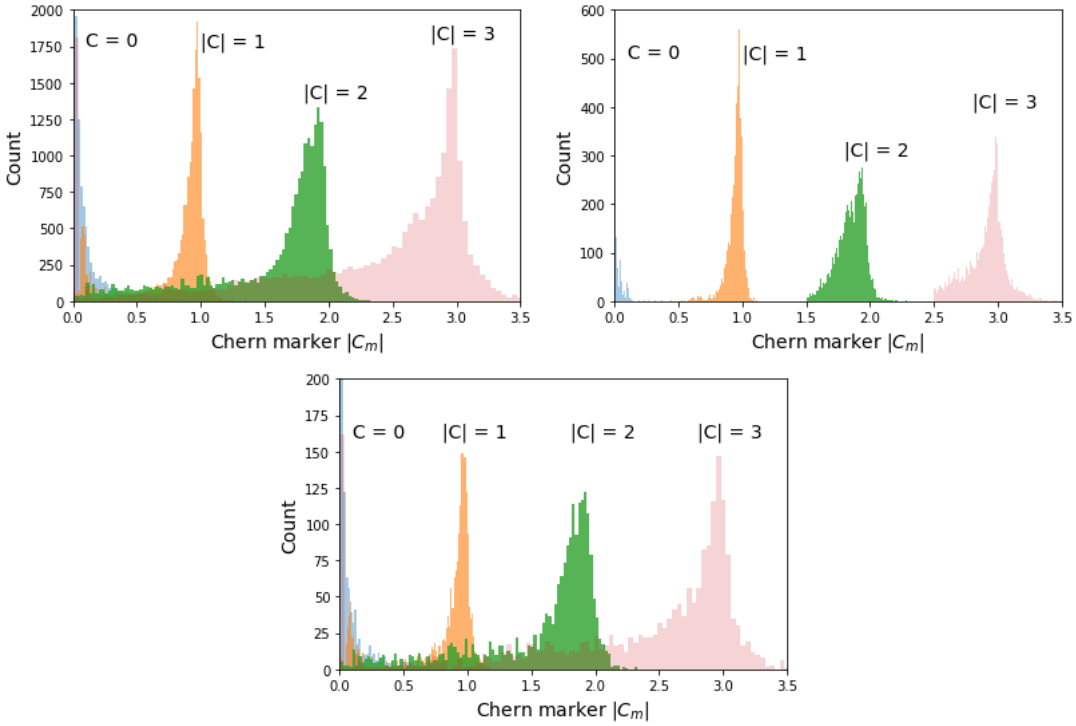

Figure 7: Chern marker $|C_m|$ histograms for *raw dataset* (top panel), *training dataset* (middle panel) and *testing dataset* (bottom panel).

5 Deep Neural network model

5.1 Neural Network architectures

Model construction, as well as model training, was prepared using *Keras v. 2.4.3* library with *TensorFlow v. 2.3.1* library as a backend. We consider three Neural Network architectures (Figure 8 top panel):

- Model A: Fully Connected Neural network
    1. Input: vector of size $24^2 \times 1$
    2. Fully connected dense layer of size 256 with $ReLU$ activation function
    3. Fully connected dense layer of size 128 with $ReLU$ activation function
    4. Dropout layer (dropout equal to 0.5)
    5. Output: vector of size 4×1
- Model B: Convolutional Neural Network with single hidden layer
    1. Input: image of size 24×24
    2. 2D Convolutional layer with 64 channels, kernel 3×3, stride 1 with same padding and $ReLU$ activation function
    3. 2D MaxPooling layer with pool size 2×2 and stride 2
    4. Flatten layer
    5. Dropout layer (dropout equal to 0.5)
    6. Output: vector of size 4×1

- Model C: Convolutional Neural Network with two hidden layers

  1. Input: image of size 24×24
  2. 2D Convolutional layer with 64 channels, kernel 3×3, stride 1 with same padding and $ReLU$ activation function
  3. 2D MaxPooling layer with pool size 2×2 and stride 2
  4. 2D Convolutional layer with 32 channels, kernel 3×3, stride 1 with same padding and $ReLU$ activation function
  5. 2D MaxPooling layer with pool size 2×2 and stride 2
  6. Flatten layer
  7. Dropout layer (dropout equal to 0.5)
  8. Output: vector of size 4×1

Above models are trained on *training dataset* for 100 epochs with *categorical cross-entropy* loss function and *Adam* optimization with learning rate equal to 0.001. We prepare 10 independent training runs and store models at each run at each epoch. Figure 8 (bottom panel) presents mean value, and standard deviation, of accuracy prediction as a function of training epochs, both on *training* and *validating datasets*, obtained for 10 different training runs. Overall accuracy for *validating dataset* reaches ≥ 0.95, however there exist visible differences between models. The simplest fully connected Model A has visibly lower accuracy prediction for *validating dataset* comparing to *training dataset*, contrary to Model B and C, where the accuracy for both datasets is almost the same. Additionally, a standard deviation of the accuracy at a given epoch in Model C is approximately two times smaller than in Model A. However, all three models give almost perfect prediction both on *training* and *validating* datasets.

5.2 Neural Network predictions

We use trained Neural Networks to predict bulk Chern number C for different disorder amplitudes V_0/δ_0. Figure 9 presents performance of three different models against disorder amplitude. All models predict bulk Chern numbers similarly well for disorder amplitudes $V_0/\delta_0 < 1$, which were included in the *training dataset*. Non-topological phases with $C = 0$ are almost perfectly well recognized, which is a trivial effect. Phases with $|C| = 1$ and $|C| = 2$ are identified with accuracy exceeding 0.8, while phases with $|C| = 3$ are predicted with accuracy slightly below 0.8. Decreasing prediction accuracy with increasing bulk Chern number is related to finite-size effects, and we expect that diagonalization on larger square lattice will improve prediction accuracy for $|C| = 3$.

Differences between considered models are clearly visible for LDOS with disorder amplitudes above $V_0/\delta_0 > 1$, which were not included in *training dataset*. Accuracy prediction of bulk Chern number rapidly drops in Model A, while Model B gives slightly better accuracy prediction for $|C| = 1$, and equally worse for $|C| = 2, 3$. Model C, however, gives good accuracy prediction for $|C| = 1$ even for large disorder amplitudes ($\sim$0.8), and slightly better accuracies for $|C| = 1, 2$ comparing to Models A and B.

The outperformance of Model C over Models A and B is also presented in Figure 10 containing confusion matrices for different disorder amplitudes V_0/δ_0 (averaged over different training runs and epochs). The diagonal structure is preserved for all considered models for $V_0/\delta_0 < 1$, however for larger disorder amplitudes only for Model C. This fact indicates that Convolutional Neural Networks perform better on the considered tasks in comparison to fully-connected dense architectures.

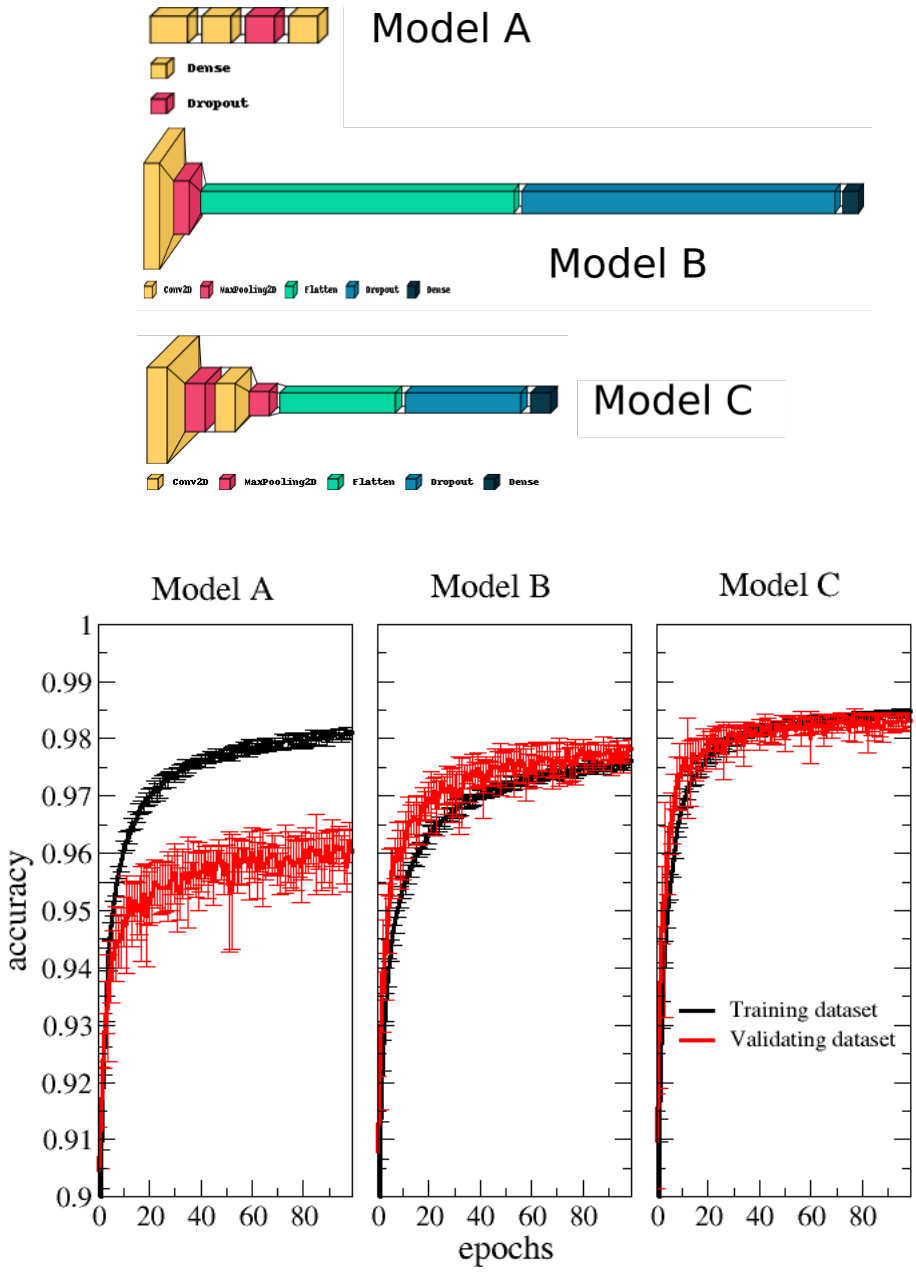

Figure 8: Top panel: Visualization of the considered Neural Network architectures: Model A contains 181124 trainable parameters, Model B contains 37508 trainable parameters and Model C contains 23716 trainable parameters. Bottom panel: Accuracy of Neural Network predictions on *training* and *validating datasets*, as a function of epochs, averaged over 10 independent training runs.

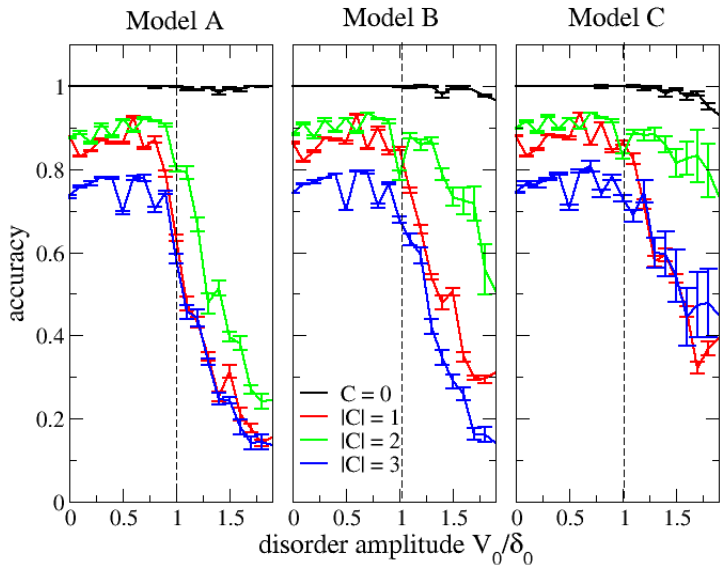

Figure 9: Accuracy of Neural Network predictions as a function of disorder amplitude V_0/δ_0 for different bulk Chern numbers C. Models were trained on data containing disorder amplitudes $V_0/\delta_0 < 1$ while testing was prepared on data with disorder $V_0/\delta_0 < 2$. Accuracy of three different models is comparable for $V_0/\delta_0 < 1$, while Model C performs better for larger disorder amplitudes, comparing to Models A and B. Almost perfect accuracy for $C = 0$ indicates the fact that that non-topological states are trivial to recognize. Additionally, one can indicate decrease accuracy with the increasing bulk Chern number C, being the artefact of the finite system size.

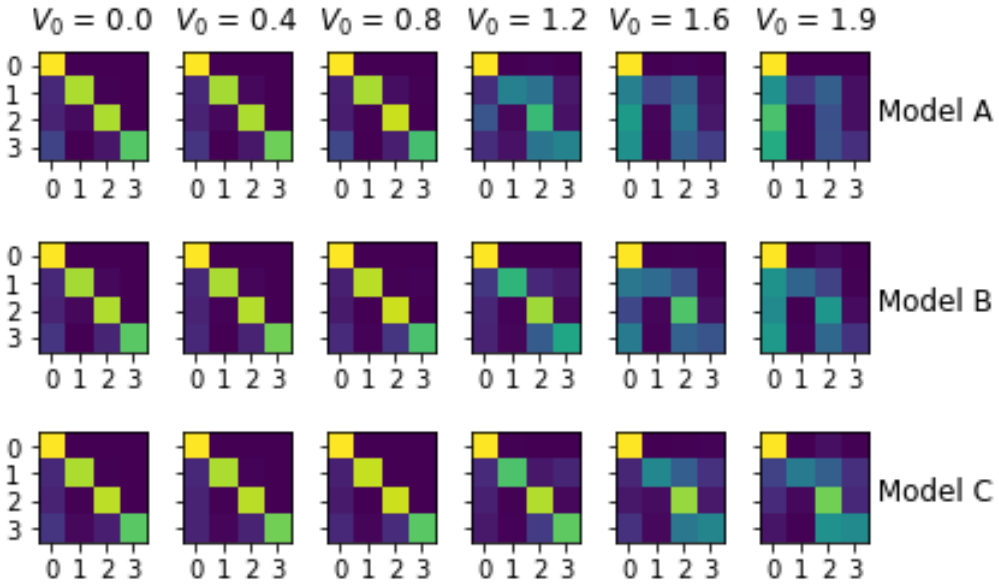

Figure 10: Confusion matrix averaged over 100 epochs and 10 training runs for three different Neural Network architectures at different disorder potential V_0 (in units of δ_0). For disorder amplitudes below $V_0 = 1$ all three models have similar structure of the confusion matrix. However, at larger disorder amplitudes Model C still preserves diagonal structure, while for Model A and B structure is almost lost.

6 Conclusion

In the presented tutorial we have focused on using Deep Neural Networks to extract topological invariants of an artificial topological Hamiltonian based on Local Density of States measurements in the presence of imperfections, modeled by introducing a random potential with different disorder amplitudes. We considered three Neural Network architectures (Fully-Connected network with two hidden layers and two Convolutional Neural Networks with one- and two- hidden layers, respectively) and indicate their predictive power in determining Chern numbers based on local measurements for considered artificial topological Hamiltonian. We conclude that Convolutional Neural Networks are a good choice of network architectures designed to identification of topological invariant from two-dimensional LDOS measurements. Additionally we analyze performance of Neural Networks on *testing dataset* containing samples with disorder amplitudes which are not included in the *training dataset*. We show that Convolutional Neural Network with two hidden layers outperforms other considered models.

We should notice that the considered topological Hamiltonian is artificial. To proceed in the research direction of topological invariants measurements, we should test Neural Networks on physical models, such as a Shiba lattice, being the microscopic model of p-wave topological superconductors [**?**, **?**, **?**], supporting topological phases with large Chern numbers. Such an approach, *i.e.* training Neural Network on local data generated for an artificial topological Hamiltonian, and testing on the physical model, will open the possibility to measure topological invariants of the new exotic topological materials without knowing their microscopic description explicitly.

Acknowledgements

Acknowledgements should follow immediately after the conclusion.

References

[1] T. J. Sejnowski, *The Deep Learning Revolution: Machine Intelligence Meets Human Intelligence*, The MIT Press (2018).

[2] B. Ramsundar, P. Eastman, P. Walters and P. V., *Deep Learning for the Life . Applying Deep Learning to Genomics, Microscopy, Drug Discovery, and More*, O'Reilly (2019).

[3] M. F. Dixon, I. Halperin and P. Bilokon, *Machine Learning in Finance: From Theory to Practice*, Springer (2020).

[4] J. Eisenstein, *Introduction to Natural Language Processing*, The MIT Press (2019).

[5] R. S. Sutton and A. G. Barto, *Reinforcement Learning. An Introduction*, Bradford Books (2018).

[6] H.-Y. Huang, R. Kueng and J. Preskill, *Information-theoretic bounds on quantum advantage in machine learning*, Phys. Rev. Lett. **126**, 190505 (2021), doi:10.1103/PhysRevLett.126.190505.

[7] G. Carleo, I. Cirac, K. Cranmer, L. Daudet, M. Schuld, N. Tishby, L. Vogt-Maranto and L. Zdeborová, *Machine learning and the physical sciences*, Rev. Mod. Phys. **91**, 045002 (2019), doi:10.1103/RevModPhys.91.045002.

[8] V. Dunjko and H. J. Briegel, *Machine learning & artificial intelligence in the quantum domain: a review of recent progress*, Reports on Progress in Physics **81**(7), 074001 (2018), doi:10.1088/1361-6633/aab406.

[9] J. Carrasquilla, *Machine learning for quantum matter*, Advances in Physics: X **5**(1), 1797528 (2020), doi:10.1080/23746149.2020.1797528, https://doi.org/10.1080/23746149.2020.1797528.

[10] Z. Liu and M. Tegmark, *Machine learning conservation laws from trajectories*, Phys. Rev. Lett. **126**, 180604 (2021), doi:10.1103/PhysRevLett.126.180604.

[11] H. Fan, J. Jiang, C. Zhang, X. Wang and Y.-C. Lai, *Long-term prediction of chaotic systems with machine learning*, Phys. Rev. Research **2**, 012080 (2020), doi:10.1103/PhysRevResearch.2.012080.

[12] Y. Z. Wan and T. P. Sapsis, *Machine learning the kinematics of sphericalparticles in fluid flows*, J. Fluid. Mech **857**, 1 (2018).

[13] A. Canabarro, F. F. Fanchini, A. L. Malvezzi, R. Pereira and R. Chaves, *Unveiling phase transitions with machine learning*, Phys. Rev. B **100**, 045129 (2019), doi:10.1103/PhysRevB.100.045129.

[14] W. Zhang, J. Liu and T.-C. Wei, *Machine learning of phase transitions in the percolation and xy models*, Phys. Rev. E **99**, 032142 (2019), doi:10.1103/PhysRevE.99.032142.

[15] A. V. Uvarov, A. S. Kardashin and J. D. Biamonte, *Machine learning phase transitions with a quantum processor*, Phys. Rev. A **102**, 012415 (2020), doi:10.1103/PhysRevA.102.012415.

[16] K. Kottmann, P. Huembeli, M. Lewenstein and A. Acín, *Unsupervised phase discovery with deep anomaly detection*, Phys. Rev. Lett. **125**, 170603 (2020), doi:10.1103/PhysRevLett.125.170603.

[17] J. Romero, J. P. Olson and A. Aspuru-Guzik, *Quantum autoencoders for efficient compression of quantum data*, Quantum Science and Technology **2**(4), 045001 (2017), doi:10.1088/2058-9565/aa8072.

[18] I. A. Luchnikov, A. Ryzhov, P.-J. Stas, S. N. Filippov and H. Ouerdane, *Variational autoencoder reconstruction of complex many-body physics*, Entropy **21**(11) (2019), doi:10.3390/e21111091.

[19] D. Ballarini, A. Gianfrate, R. Panico, A. Opala, S. Ghosh, L. Dominici, V. Ardizzone, M. De Giorgi, G. Lerario, G. Gigli, T. C. H. Liew, M. Matuszewski *et al.*, *Polaritonic neuromorphic computing outperforms linear classifiers*, Nano Letters **20**(5), 3506 (2020), doi:10.1021/acs.nanolett.0c00435, PMID: 32251601, https://doi.org/10.1021/acs.nanolett.0c00435.

[20] R. Mirek, A. Opala, P. Comaron, M. Furman, M. Król, K. Tyszka, B. Seredyński, D. Ballarini, D. Sanvitto, T. C. H. Liew, W. Pacuski, J. Suffczyński *et al.*, *Neuromorphic binarized polariton networks*, Nano Letters **0**(0), null (0), doi:10.1021/acs.nanolett.0c04696, PMID: 33635656, https://doi.org/10.1021/acs.nanolett.0c04696.

[21] N. L. Holanda and M. A. R. Griffith, *Machine learning topological phases in real space*, Phys. Rev. B **102**, 054107 (2020), doi:10.1103/PhysRevB.102.054107.

[22] P. Zhang, H. Shen and H. Zhai, *Machine learning topological invariants with neural networks*, Phys. Rev. Lett. **120**, 066401 (2018), doi:10.1103/PhysRevLett.120.066401.

[23] N. Sun, J. Yi, P. Zhang, H. Shen and H. Zhai, *Deep learning topological invariants of band insulators*, Phys. Rev. B **98**, 085402 (2018), doi:10.1103/PhysRevB.98.085402.